Fuel 407 (2026) 137328

Contents lists available at ScienceDirect

Fuel

journal homepage: www.elsevier.com/locate/fuel

Full Length Article

Machine learning-aided multi-objective optimization of Tesla valve-based membraneless electrolyzer efficiency

Mohammadali Zoljalali, Richard Ahorsu, Francesc Díaz, Magdalena Aguiló, Xavier Mateos *

University Rovira i Virgili (URV), Physics and Crystallography of Materials (FiCMA) research group, Marcel·lí Domingo 1, 43007 Tarragona, Spain

A B S T R A C T

Hydrogen (H_2) is an attractive fuel due to its high specific energy and zero direct carbon emissions. Membraneless electrolyzers (MEs) offer a lower-cost route to hydrogen production, but their operation is complex and current efficiencies are modest. Although multi-objective optimization is widely used, its heavy compute demands and weak integration with modern learning methods limit scalability and adaptability. We introduce a practical, ML-guided way to design Tesla-valve (TV) membraneless electrolyzers by building diodicity (Di) directly into the geometry search. Using multilayer-perceptron surrogates trained on 150 high-fidelity simulations ($R^2 > 0.95$), we link four design knobs (We, Wc, Wd, Di) to pressure drop (Δp) and ohmic loss. A Genetic Algorithm (GA)-based multi-objective search over realistic ranges delivers 60 Pareto-optimal designs that make the Δp–ohmic trade-off explicit; TOPSIS then selects a balanced geometry (We = 1.708 mm, Wc = 0.200 mm, Wd = 1.012 mm, Di = 1.618) with ohmic loss 4.069 V and Δp 6.169 Pa. The approach delivers faster, lower-cost design maps and is supported by experimental checks, pointing to an actionable route for scalable, interpretable optimization of sustainable hydrogen production.

1. Introduction

In recent years, hydrogen has emerged as a promising alternative to conventional energy sources amid the growing urgency to mitigate climate change [1]. Electrolyzers, which produce green hydrogen via water splitting, are central to this transition. These systems typically comprise three main components: electrodes, membranes, and an electrolyte [2]. Among these, the membrane or diaphragm plays a critical role in separating the produced gases and remains a vulnerable component in terms of fabrication, operation, and maintenance. Membrane performance is particularly influenced by parameters such as flow rate, pH, and temperature [3].

To address these challenges, researchers have proposed alternative designs that eliminate the need for traditional membranes. Membraneless electrolyzers (ME), utilize microfluidic principles to achieve hydrogen and oxygen separation without diaphragms[4,5]. ME systems rely on inertial effects or tailored geometries to guide gas bubbles and maintain separation[6]. These systems are commonly classified into two categories: (i) the “flow-by“ electrolyzers that separate bubbles using a Hagen Poiseuille type flow [7] where bubbles reach an equilibrium position influenced by the flow rate, size, and wall interactions [8,9] and the plume of the produced bubbles are decisive in electrolyzer design [10]. And (ii) the ”flow-through“ electrolyzers that allow the electrolyte to pass through porous or mesh-structured electrodes. Additional variants have been reported, though they are less extensively studied [11,12]. These membraneless electrolyzers experience high pressure drop although they have good potential for scalability [13,14].

Membraneless electrolyzers are simple and cost-effective to fabricate; however, their working principles are complex, influenced by multiple interdependent parameters, each affecting the global efficiency [2]. The efficiency of a membraneless electrolyzer depends on parameters such as pressure drop, overpotential, and the amount of hydrogen generation. However, these parameters exhibit trade-offs. Thus, improving one can adversely impact another. Our Tesla-valve (TV)-based electrolyzer, which employs the concept of diodicity: that’s permitting electrolyte flow in one direction displays similar trend. Leveraging the diodicity of the Tesla connectors and swapping electrode placement improves H_2 bubble detachment and reduce overpotential swings, thereby improving the H_2 production rate by ~ 13 % when the cathode is placed in the lower channel [6]. The 13 % improvement in H_2 production obtained from the diodicity effect highlights the subtle, geometry-sensitive benefits of Tesla-valve-based electrolyzers and therefore demands careful optimization to realize meaningful gains. Changes in the design of TV electrolyzers contribute to differing trends in pressure drop and ohmic loss, a conflict well reported in the literature [2,15]. Consequently, because the Tesla valve features are tunable (angles, spacing, link widths), diodicity becomes a governing design knob to co-optimize pressure drop, bubble removal, gas separation and overall efficiency surpassing other plain flow-by passive structures.

To navigate these coupled effects, we formulate the design of the TV

* Corresponding author.
E-mail address: xavier.mateos@urv.cat (X. Mateos).

https://doi.org/10.1016/j.fuel.2025.137328
Received 29 August 2025; Received in revised form 13 October 2025; Accepted 24 October 2025
Available online 27 October 2025
0016-2361/© 2025 The Authors. Published by Elsevier Ltd. This is an open access article under the CC BY-NC license (http://creativecommons.org/licenses/by-nc/4.0/).

electrolyzer as a multi-objective optimization problem.

Multi-objective optimization (MOO) is a powerful tool in cases where two or more objectives are in conflict or are interdependent [16]. In such situations, where parameters or objectives are interdependent, the objectives cannot be optimized simultaneously, making a single optimal solution unfeasible [17]. Instead, MOO yields a set of Pareto-optimal solutions, each representing a trade-off that contributes reasonably to system efficiency. Important factors in calculating electrolyzer efficiency include chemical power stored as hydrogen, fluidic power, and overpotential can be covered within method. This method has recently gained attention in reactors design and efficiency studies [18,19]. Exploring membrane electrode assembly (MEA) in PEMs to improve cost and durability has drawn attention to itself. [20,21]. Nikzad et al. explored operating variables such as feeds, temperatures, and membrane thickness, and subsequently applied MOO to resolve competing goals across the coupled reactions, identifying Pareto-optimal operating points where NH_3 and methyl formate yields reach 20.3 % and 24.1 %, respectively. MOO serves as the defining engine that translates the reactor's thermodynamic advantages into practical, balanced performance targets, quantifying the trade-offs and guiding selection of the best compromise operating conditions [22]. In another study, the authors use multi-objective optimization across three cases, it identifies trade-offs and operating points that maximize aromatics/research octane number (RON) and H_2 while minimizing light ends, with the best objective set found to be maximizing aromatics (octane) and minimizing light ends [23]. In practice, MOO lets operators tune conditions to prioritize either higher H_2 yield or higher octane delivering better product slates and efficiency without sacrificing environmental goals.

Incorporating machine learning (ML) and/or deep learning (DL) models as surrogates in MOO is computationally and resource-efficient approach to solving complex momentum, energy, and mass transfer equations [24,25]. For electrolyzers, high-fidelity simulation is computationally intensive: ML and DL models can simplify these processes and reduce computational costs in optimization [26]. Surrogates' integration accelerates policy training by replacing expensive reactor simulations, enabling constraint-aware exploration and yielding superior Pareto fronts (+65.69 % hypervolume, −66.26 % IGD vs. a genetic algorithm; TOPSIS = 0.9699) as demonstrated by Shahriari et al. [27]. ML-driven method delivers clear, scalable optimization for sustainable hydrogen production and also applies to other industrial energy systems.

In this work, we develop a machine learning-aided framework to optimize the geometry of a Tesla valve-based membraneless electrolyzer. Tesla valves are incorporated into the design to establish ion transfer and promote directional flow, aiding in the separation of hydrogen and oxygen gases. A dataset linking geometrical parameters to performance metrics (pressure drop, hydrogen production, and ohmic loss) was generated from high fidelity CFD simulations using Tertiary Current Distribution Interface. A multilayer perceptron artificial neural network (MLP) was trained to predict these outputs from geometry-based inputs. Notably, pressure drop and ohmic loss exhibited conflicting trends, while storage capacity was mainly dependent on electrode size. To ensure input diversity and avoid redundant geometries yielding identical diodicity, an inverse MLP-genetic algorithm (MLP-GA) module was developed to generate Tesla geometries based on target diodicity values. The trained MLP models were then integrated into a multi-objective optimization framework using a genetic algorithm to identify Pareto-optimal designs. A multi criteria decision making study was carried out and one geometry was introduced as the best option in design space.

Our objective is to simultaneously (i) minimize pressure drop and ohmic losses and (ii) maximize hydrogen production (while constraining overpotential and gas crossover). We therefore employ a multi-objective optimization tool to map the Pareto front and identify geometries that deliver balanced performance across these competing metrics. While MOO generates a set of pareto optimal data which is the tradeoff between ohmic loss and pressure drop; it does not indicate which solution is better among all. MCDM bridges this gap by ranking the solutions based on defined criteria. The integration of MCDM is valuable in engineering problems like electrolyzers design where maximizing energy efficiency, minimizing pressure drop, and reducing ohmic loss are all critical yet competing goals. The proposed method was validated experimentally and provides a computationally efficient alternative to traditional simulation-heavy optimization approaches. To our knowledge, this is the first study to incorporate the concept of diodicity into electrolyzer design and links it to ohmic loss and pressure drop within a geometry-aware, AI-driven framework.

2. Methodology

This section describes the step-by-step approach used in the design, simulation, modeling, and MOO of the Tesla valve-based membraneles electrolyzer. The study was carried out in the same order as the actual work.

2.1. Tesla valve (TV) electrolyzers

In this work, a membraneless electrolyzer was designed to separate hydrogen and oxygen without the need for a membrane, as illustrated in Fig. 1. In this structure, 12 TV connectors are used to establish ion transfer. The difference in cross-sectional area between the main channel and the Tesla connectors allows for effective bubble separation. The geometry of the proposed membraneles electrolyzer includes four critical parameters that determine its efficiency:

(i) We: the width of the channel containing the electrodes,

(ii) Wc: the width of the Tesla connections between channels,

(iii) Wd: the distance between the connections.

(iv) Diodicity (Di): the ratio of forward to reverse flow resistance, capturing the rectification behavior of TV-electrolyzer.

These parameters were selected because they directly influence the available reaction area, ion transport path, and fluidic resistance, all of which affect efficiency. The range of these parameters which determine the design space in this study is provided in Table 1.

The geometrical bounds were selected to ensure physically meaningful operation and fabrication feasibility of the membraneless electrolyzer. Because bubble separation relies on maintaining laminar flow in microfluidic channels, the channel dimensions were constrained to the microscale. Preliminary multiphysics simulations (coupling Laminar Flow, Mixture Model, and Secondary Current Distribution in COMSOL) were used to verify that within these ranges, hydrogen and oxygen bubbles followed equilibrium trajectories without crossing into Tesla connections. The inlet gas fluxes in these simulations were defined from Faraday's law using the total current density, which provided physically consistent boundary conditions. These studies yielded an initial design framework that served as the starting point for optimization, ensuring that the chosen lower and upper limits span both practical fabrication ranges and bubble-stable operating regimes.

To generate a well-distributed and efficient set of input parameters, Latin Hypercube Sampling (LHS) was employed. Additionally, it is worth mentioning that the total length of the electrode equals the sum of the Tesla connections lengths and the distances between them.

To investigate the effect of the Di of the connections, three decisive geometrical parameters in the structure of the Tesla connections including θ, R, and L were taken into account, whose varying Di values were taken into consideration. The mentioned parameters are shown in figure 1S in Supplementary I. This configuration resulted in an MLP with seven inputs and one output, but changing three geometrical parameters of Tesla connections could yield the combinations of geometry which results in identical Di. To refrain from this problem and have a diversity in the training data, a separate algorithm was developed to generate geometries for Di values. The goal is to determine the optimal geometrical parameters that achieve a desired diodicity value. The algorithm employs a hybrid MLP-genetic algorithm (MLP-GA) structure to map

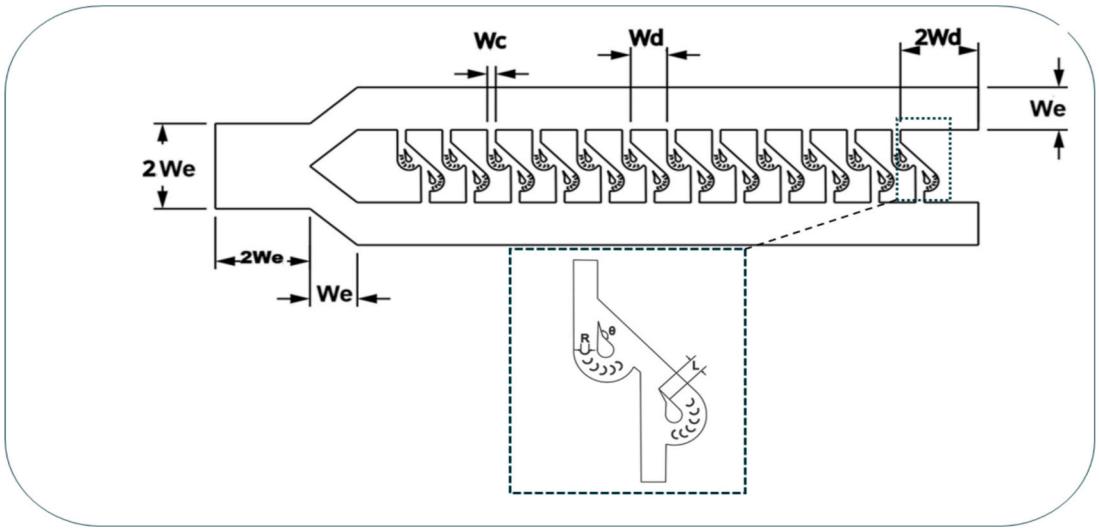


Fig. 1. Configuration of the Tesla valve base membraneless electrolyzers; We, Wc, Wd, L, θ and R, represent the width of the channel containing the electrodes, the width of the Tesla connections between channels, the distance between the connections, Length of the divider's folded segment, angle of the divider's folded segment, and Arc shape fin diameter, respectively.

Table 1
Changes of the geometrical parameters in the TV electrolyzers.

Parameter	Range of the changes
We	0.25 – 2.1 (mm)
W_c	0.04—0.2 (mm)
W_d	0.41–2.5 (mm)
Di	0.9 – 1.7

target diodicity to unique geometric parameters, (detailed in Supplementary I). Given the complex and nonlinear nature of the relationship between geometrical parameters and diodicity, a hybrid approach using an Multi-Layer Perceptron (MLP) and a Genetic Algorithm (GA) is employed. Supplementary I gives a detail explanation of this algorithm.

To study the efficiency of this system, the equation (1) will be considered [12].

$$\eta_{Conversion} = \frac{P_{Storage}}{P_{Storage} + P_{Fluidic} + P_{overpotential}} \quad (1)$$

In this equation $P_{Storage}$ is the chemical power stored in the form of hydrogen and $P_{Overpotential}$ is overpotentials corresponding to the hydrogen and oxygen evolution reactions and due to the ohmic resistance, and $P_{Fluidic\text{-}power}$ required to overcome fluidic resistance. Equations (2), 3, and 4 show equation (1) parameters in detail.

$$P_{Storage} = j.L.H.E_0 \quad (2)$$

In this equation j is current density, L is the length of the electrode, H is the height of the electrode, which is fixed in all cases, and E_0 is the thermodynamic equilibrium potential of water electrolysis, i.e. 1.23 V.

The $P_{overpotential}$ will be calculated with equation (3).

$$P_{overpotential} = jLH(|\eta_{HER}| + \eta_{OER} + \eta_{ohmic}) \quad (3)$$

While the full cell overpotential includes contributions from reaction kinetics (HER, OER) and ohmic resistance, this study focuses on the ohmic component. This choice is justified by the fact that ohmic loss is strongly dependent on channel geometry and flow distribution, while the kinetic terms remain constant under identical current density and electrode conditions.

In equation (1), $P_{Fluidic}$ can be calculated with equation (4).

$$P_{Fluidic} = \Delta P.Q \quad (4)$$

In this equation ΔP is pressure drop across the system and Q is the electrolyte flowrate.

In the mentioned Equations (2), 3, and 4, $P_{storage}$ at a constant current density change with electrode dimensions. For the two other parameters, including ohmic drop and pressure drop, the trends are contradictory.

COMSOL Multiphysics was used to model via parameter sweeps. The Tertiary Current Distribution (Nernst–Planck) module was utilized to simulate ion transport, considering diffusion, migration, and convection effects. These simulations formed the training dataset for the surrogate models. Mesh quality, boundary conditions, and physics were carefully adjusted to ensure reliable and transferable outputs. Model validation was performed by comparison against experimental data.

2.2. Simulation framework

Electrochemical species transport was modeled considering diffusion, migration, and convection as described by equation (5) [28]:

$$N_i = -D_i\nabla_{C_i} - z_i\mu_i c_i \nabla\varnothing + c_i U \quad (5)$$

where N_i, D_i, c_i, z_i, and μ_i are the flux, diffusion coefficient, concentration (not to be confused with diodicity, Di), charge number, and mobility of the species "i" in the electrolyte respectively. F, $\varnothing_l$, and u in equation (6) denote the Faradic constant, electrolyte potential and the local velocity of the electrolyte flow respectively.

Current density expression with the Nernst-Planck equation is shown in equation (6):

$$i_l = -F\left(\nabla\sum_i z_i D_i c_i\right) - F^2\nabla\varnothing_l\sum_i z_i^2 u_{m,i} + uF\sum_i z_i c_i \quad (6)$$

In current distribution interface in COMSOL, tertiary current distribution; the variation in composition of the electrolyte will be taken into consideration. Also, in this module the solution resistance and electrode kinetics will play the role. The Nernst-Plank equation will be solved to describe mass transfer considering diffusion, migration, and convection. In this module, reactant exhaustion at the electrode–electrolyte will be considered.

The solved equation for the electrode and electrolyte is following

equations (7) and (8).

$$i_s = \sigma_s \nabla \varnothing_s with \nabla . i_s = Q_s \tag{7}$$

$$i_l = F \sum_{i=1}^{n} z_i \left(-D_i \nabla c_i - z_i u_{m,i} F c_i \nabla \varnothing_l \right) with \nabla . i_l = Q_l \tag{8}$$

Equation (9) shows the electrode–electrolyte interface. Overpotential (η_m) is expressed as

$$\eta_m = \varnothing_s - \varnothing_l - E_{eq,m} \tag{9}$$

Electrolyte electroneutrality

$$\sum_i z_i c_i = 0 \tag{10}$$

Typical current density expression:

$$i_{loc,m} = i_{0,m} \left(\frac{c_{Red}}{C_{ref}} e^{\frac{\alpha_{a,m} F \eta m}{RT}} - \frac{c_{ox}}{c_{ref}} e^{\frac{-\alpha_{c,m} F \eta m}{RT}} \right) \tag{11}$$

In equation (11), $i_{0,m}$ is exchange current density at electrode m, c_{Red} and c_{ox} are concentrations of the reduced and oxidized species, C_{ref} is reference concentration, $\alpha_{a,m}$, $-\alpha_{c,m}$ are anodic and cathodic charge transfer coefficients, F is Faraday constant, η_m is overpotential at electrode m, R is universal gas constant and T is temperature.

Due to the dependence of concentration, the tertiary current distribution becomes influenced by the flow of the electrolyte and hence the availability of the reactant by mass transport. After modeling the COMSOL models, MLP models were trained based on the CFD models data.

2.3. Experimental setup

To validate the COMSOL models used for training the MLP, computational fluid dynamics(CFD) simulations were benchmarked against experimental data. The experiments were conducted for the TV-electrolyzers with a Di of 0.9. The Tesla connector width was 0.04 mm, the width of the main channel was 0.2 mm, and the distance between the Tesla connectors was 0.19 mm. The length of the electrode is calculated by the formula: N(Wc) + (N + 1)(Wd), where N is the number of Tesla connectors.

The mentioned structure was fabricated in the clean room through two distinct and parallel processes. Sputtering was the method used to fabricate the electrode part. In this process, a glass slide was spin-coated with photo sensitive resin AZ1505 and, after post-baking, was exposed to X-ray using a photomask with the electrode geometry. Then, a layer of 10 nm Titanium and 100 nm Platinum were sputtered onto the glass.

In parallel, a silicon wafer was spin-coated with SU82035 and, after baking, was exposed to X-ray lithography. After post-baking and developing the sample, the mold was ready. In the next step, the PDMS solution was poured onto the mold, and after 1 h in the oven at 80 °C, the channel part was obtained. The assembly was completed by bonding the PDMS part with the glass slide on which the electrodes had been sputtered. The fabrication process is shown in Fig. 2. The fabricated membraneless electrolyzer working under conditions of 300 mA·cm^{-2} and 80 mL·h^{-1} is shown in Fig. 3.

In the experiment, an Elveflow OB1 MK4 was used to pump 0.5 M H_2SO_4 as the electrolyte. A potentiostat (Ivium Vertex.C) was used to apply voltage and perform electrochemical analysis. For the validation of the COMSOL model, a linear sweep voltammetry (LSV) test was carried out at a flow rate of 80 mL h^{-1}.

2.3.1. Multilayer perceptron neural network

Artificial neural networks are efficient tools for precise modelling of the data changing patterns in nonlinear multivariate systems [29].

In this work, MLPs were used not only to approximate simulation results but also to significantly reduce computational time during optimization. Each MLP replaces a full physics-based model, enabling faster exploration of the design space.

Before training, all input and output variables (ohmic loss, pressure drop, storage) were normalized to the range [0,1]. To normalize the data equation (12) was used.

$$x' = \frac{x - x_{min}}{x_{max} - x_{min}} \tag{12}$$

In equation (12), x is the original variable, x_{min} and x_{max} are the minimum and maximum values of that variable in the dataset, and x′ is the normalized value. This preprocessing ensured that all variables contributed equally during training.

The general architecture of an MLP consists of three principal elements: the input layer, the hidden layer(s), and the output layer. These layers are interconnected by weighted connections which are responsible for modifying the transmitted signals between the layers. These weights play a significant role in determining the effectiveness of each layer [30].

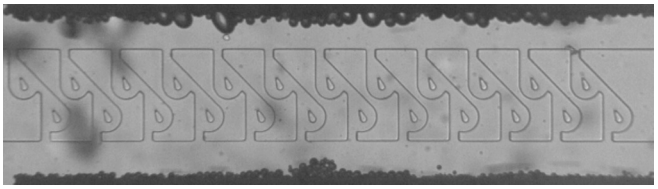


Fig. 3. Microscope image of the working electrolyzer at 300 mA, cm^{-2} and 80 ml h^{-1}.

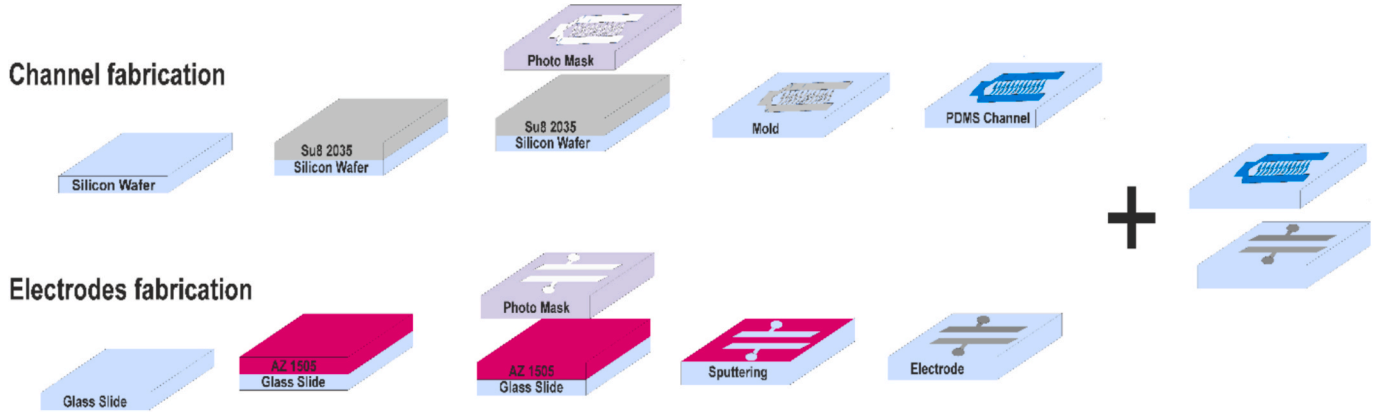


Fig. 2. Sketch of the fabrication methodology.

Equation (13) stands for the final output of each MLP artificial neural network [31]:

$$Y = F_l\left\{\sum_{j=1}^{n} W_{kj}\left[F_t\left(\sum_{i=1}^{m} W_{ji}X_i + b_j\right)\right] + b_k\right\} \quad (13)$$

In this equation, Y is the final output of the network, F_l is transfer function for the output layer, n is the number of neurons, m is the number of input variables, i, j,k refer to input, hidden, and output layers, respectively. The F_l transfer function has been used for the output layer of MLP [32].

In this study, we applied the Levenberg–Marquardt (LM) algorithm for training, as it's well-suited for solving nonlinear problems efficiently [33,34]. Once trained, the MLP models serve as surrogate models to support a multi-objective optimization process.

2.3.2. Multi-objective optimization

From our earlier observations, ohmic loss and pressure drop pull in opposite direction; hence, improving one usually makes the other worse. To balance this trade-off, a MOO was applied using the trained MLP models as fast estimators.

The MOO refers to finding the best solution for a problem that has contradictory parameters [35].

A practical approach in MOO is to identify a Pareto-optimal set, representing solutions that satisfy balanced trade-off between objectives. In mathematical terms it can be written in the form of equation (14):

$$min/\max f_1(x), f_2(x), \cdots, f_n(x) \quad (14)$$

$$subjectto : x \in U$$

In this equation x is the solution, n represents the number of objective functions, U is the set of function and min/max is combined object operations.

In this framework, a solution is considered Pareto-optimal if no other solution exists in the possible space that ameliorates one objective without negatively affecting at least one other [36]. For many optimizations problems the number of Pareto-optimal solutions is infinite [37]. In complex systems, such as this study which is using MLP as surrogated model, finding the pareto optimal set, which consists of non-dominated solutions, is computationally overwhelming. The number of optimal Pareto solutions grows exponentially with the complexity of the system. Also processing all the solutions demands a high number of resources.

To overcome this challenge, GA which is a type of evolutionary algorithm inspired by natural selection, was employed. The GA process works in six steps [38].

1. Initialization, during which a population of potential solutions known as chromosomes or individuals is generated.
2. Each chromosome or individual in the generated population is evaluated using a fitness function (or objective function in MOO) to evaluate how it solves the problem.
3. Chromosomes or individuals with better fitness (better solutions) have more chances to be selected to reproduce the next generation.
4. Selected pairs undergo a cross over process. This step contributes to producing new individuals (solution) with parents' characteristics.
5. To refrain from getting stuck in local optimum random mutation is applied to the community offspring.
6. The offspring (new generation) replaces the old population, and the process is repeated. Over successive generations, the population evolves toward better solutions.

The genetic algorithm explores the design space using surrogate model predictions instead of solving physical equations, allowing faster evaluation. The final solutions form a Pareto front a set of designs where improving one objective requires compromising another.

In MOO, GAs handle multiple conflicting objectives. In fitness assignments, a solution is recognized as a Pareto-dominated solution if it is not worse in all objectives and strictly better in at least one objective. The selection of the solutions is based on Pareto ranking, in which solutions with better ranks and more diverse positions are preferred [39]. It is worth mentioning that although in standard GA, cross over and mutation are applied to increase diversity and evolve the population; in MOO the goal is to find solutions across the entire population [40]. The complete workflow is summarized in Fig. 4, which illustrates both the inverse ANN + GA framework for diodicity prediction and the main optimization pipeline from CFD to MLP surrogate models and MOO–MCDM.

2.3.3. Multicriteria decision making (Topsis)

Multi-criteria decision making (MCDM) is a method used to evaluate and choose between different options when several important factors need to be considered at the same time. In this study, MCDM was applied to select the optimal design from Pareto front by balancing trade-off between pressure drop and ohmic loss. MCDM assists in organizing the criteria involved, giving them importance (weights), and comparing the options fairly and balanced decision-making.

One popular method in MCDM is TOPSIS (Technique for Order Preference by Similarity to Ideal Solution). The fundamental concept of TOPSIS is that the best alternative should have the shortest geometric distance from the ideal solution (the best value for each criterion) and the greatest distance from the worst solution (the worst value for each criterion).

3. Result and Discussion

3.1. CFD model validation

Before training the MLP models, it was important to validate the COMSOL simulation setup against experimental data to ensure accuracy. This validation step gives confidence that the simulation outputs used for training accurately reflected real system behavior.

In the developed COMSOL model, the Tertiary Current Distribution (Nernst–Planck interface) was employed to take account for convection in the ion transfer mechanisms. In this interface, the kinetic expressions include both activation and concentration overpotentials. By this approach, all electroactive species in the electrolyte are considered. In the simulation, all solid surfaces were set to a no-slip boundary condition. For the inlet, a Dirichlet boundary condition was used, which specifies the value of the inlet solution, in this case, 0.5 M H_2SO_4. For the solid surfaces (except the electrode), a zero-flux Neumann condition was applied. On the electrode surface, the concentration of H_2SO_4 was considered zero due to the fast reaction rate at that interface. To ensure the accuracy and reliability of the simulation results, a mesh consistency analysis was carried out. The computational domain was discretized using a finite element mesh, with careful attention to the size and distribution of the mesh elements. The mesh was refined in regions with high gradients, such as near the electrode surface, to capture detailed variations in concentration and potential.

A mesh independence study was conducted to confirm that the simulation results were unaffected by the mesh size. The current density at 3 V and 80 $mL{\cdot}h^{-1}$ was considered as the criterion to study mesh independence. The results indicated that above 25,938 elements, the mesh size no longer affected the model output. To validate the CFD framework, simulated current density–voltage characteristics were compared with experimental data (Fig. 5-a). The good agreement confirms the credibility of the model and justifies its use for dataset generation and ANN training.

The mesh consisted of 16,627 vertices, with a combination of 21,156 triangular elements and 4,782 quadrilateral elements. Additionally, there were 2,704 edge elements and 289 vertex elements, resulting in a

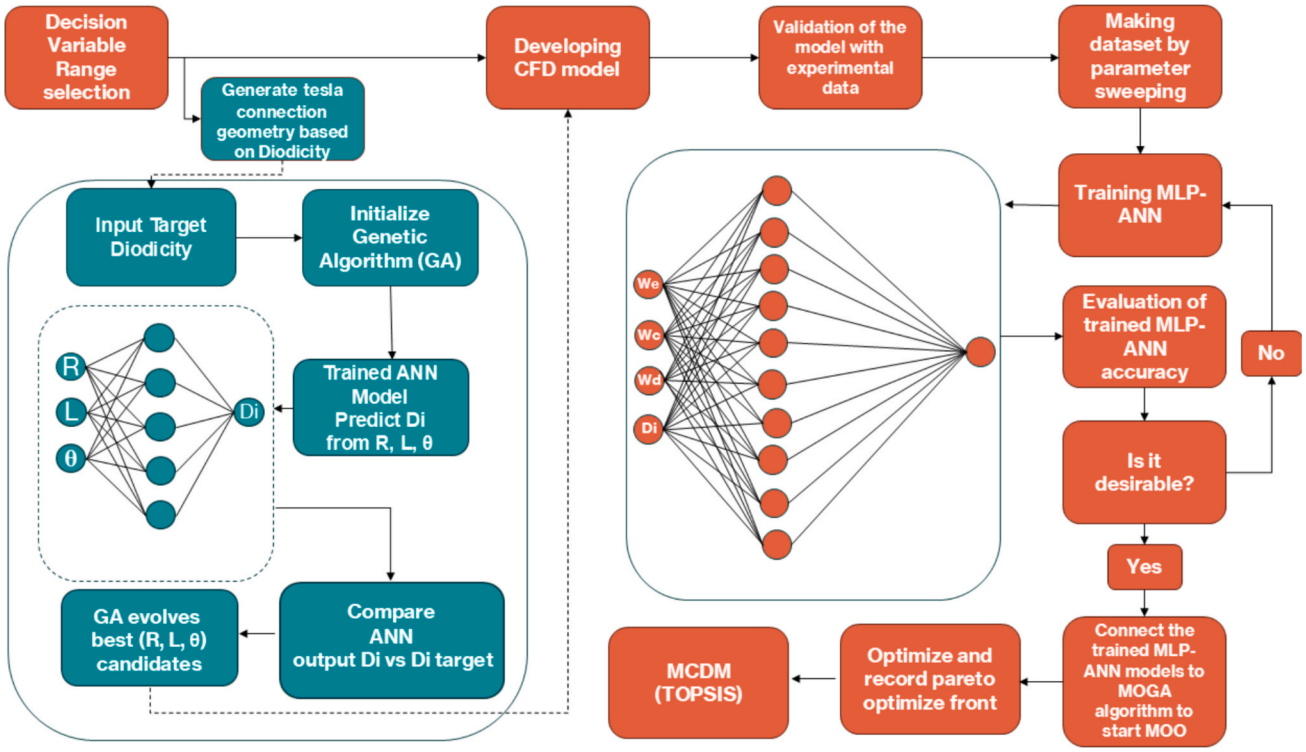


Fig. 4. Block diagram illustrating the methodology used in this work.

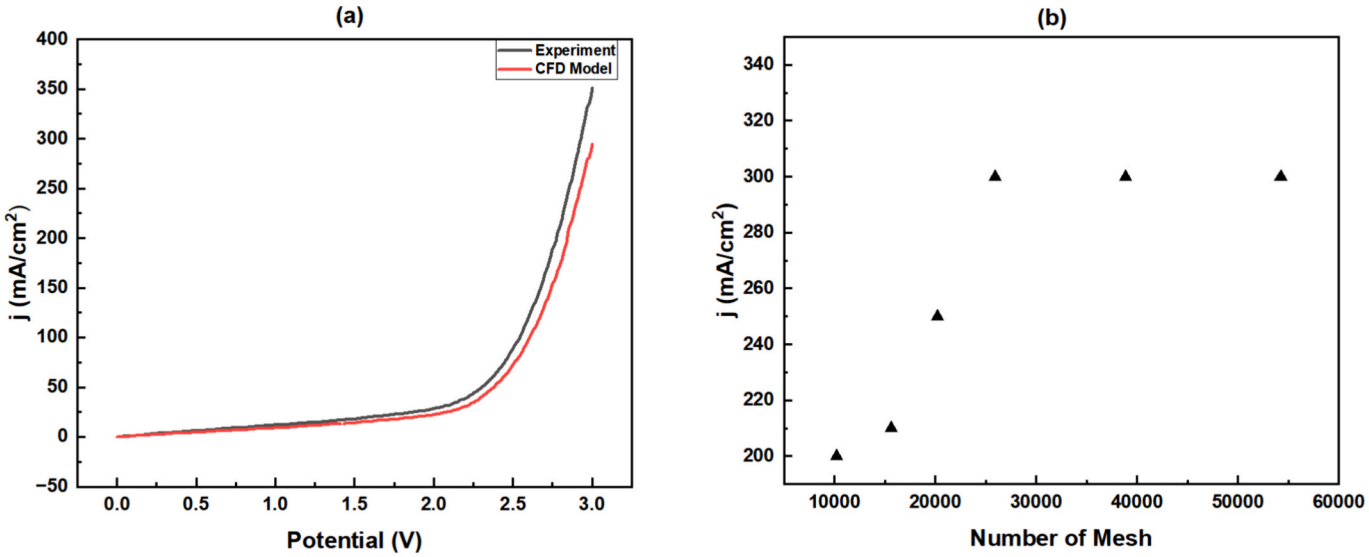


Fig. 5. A. comparison of simulated polarization curve with experimental data for validation of the cfd model. b. effect of amount of mesh on the current density (mesh independency effect).

total of 25,938 elements. The quality of the mesh was evaluated using the skewness criterion. The minimum mesh quality was 0.598, and the average mesh quality was 0.7991. A denser mesh was used on the Tesla valve connectors and electrode surfaces, where rapid changes in concentration occur. Fig. 5-b shows the results of the mesh independence study. This figure shows that when the number of meshes are more than 25000, the current density does not change significantly.

A grid convergence study was conducted using three mesh refinement level. Table 2 summarizes the effect of mesh refinement on principal performance metrics of electrolyzers. The grid convergence index was calculated based on ASME guidelines. The refinement ratio was considered. GCI values for all parameters. (safety factor Fs = 1;

Table 2
Mesh convergence study for the Tesla valve-based membraneless electrolyzer model. Three mesh refinement levels (coarse, medium, fine) were evaluated for pressure drop, ohmic loss, and current density. Grid Convergence Index (GCI) values were calculated following ASME guidelines with a safety factor of 1.25.

Parameter	Mesh number			GCI(%)
	15,606	25,908	38,858	
Pressure drop	16.03	15.95	15.91	0.32
Ohmic loss	1.74	1.72	1.71	2.1
Current density (Storage)	210	300	305	0.12

refinement ratio based on grid spacing inferred from element counts). As summarized in Table 2, GCI on the fine mesh was below 3 % for all quantities (0.32 % for pressure drop, 2.1 % for ohmic loss, 0.12 % for current density). This result is consistent with Fig. 5-b, current density stabilizes beyond ~ 25 k elements.

The coupled set of governing equations (laminar flow, mixture model, and secondary current distribution) was solved using a fully coupled Newton method. A direct linear solver (PARDISO) was employed. The initial damping factor was set to 1, with a minimum damping factor of 1×10^{-6}. Restrictions for step-size update and increase were 10 and 1, respectively, with recovery damping factor set to automatic (0.75). Automatic scaling factors in weights were enabled. Convergence was based on a tolerance criterion, with a maximum of 50 nonlinear iterations allowed.

3.2. MLP

With validated simulation data, the next step was to train machine learning models capable of predicting performance metrics. This section discusses how the MLPs were configured and the verification of their accuracy. The dataset was randomly divided into training (70 %), validation (15 %), and testing (15 %) subsets, which is a commonly used ratio in machine learning to balance generalization and robustness. These parameters play an important role in the development of a MLP model [38].

The MLPs were trained using the Levenberg–Marquardt algorithm. The training step size is adaptively controlled by the damping parameter μ, which is ($\mu = 0.001$, $\mu_{dec} = 0.1$, $\mu_{inc} = 10$, $\mu_{max} = 1 \times 10^{10}$). Hidden layers used the sigmoid activation function, and the output layer used a linear activation function.

In this architecture, the number of neurons in the input layer was set equal to the number of input parameters, which was four in this study. For the output layer contained a single neuron. The number of neurons in the hidden layer is a decisive factor in the efficiency of the trained MLP. Fig. 6 shows the R^2 and MSE values for the three different MLPs as a function of the number of neurons. The architecture for all three MLPs considered one hidden layer, which gave acceptable performance based on R^2 and MSE.

Fig. 6 illustrates the effect of hidden-layer neuron number on MLP performance for (a) storage, (b) ohmic loss, and (c) pressure drop. The selected architecture represents the optimal compromise, avoiding both underfitting at very low neuron numbers and overtraining at larger network sizes.

All three models have an R^2 of more than 0.95 and were deemed reliable surrogate models. This architecture provided an effective balance between model complexity and generalization. With R^2 values above 0.95, the trained MLPs were considered reliable enough to replace full CFD simulations during the optimization process.

To assess potential overfitting or underfitting, learning curves were analyzed for the three surrogate models in Fig. 7. In each case, the training, validation, and test errors decrease rapidly in the first few epochs and stabilize at low values without divergence. The validation

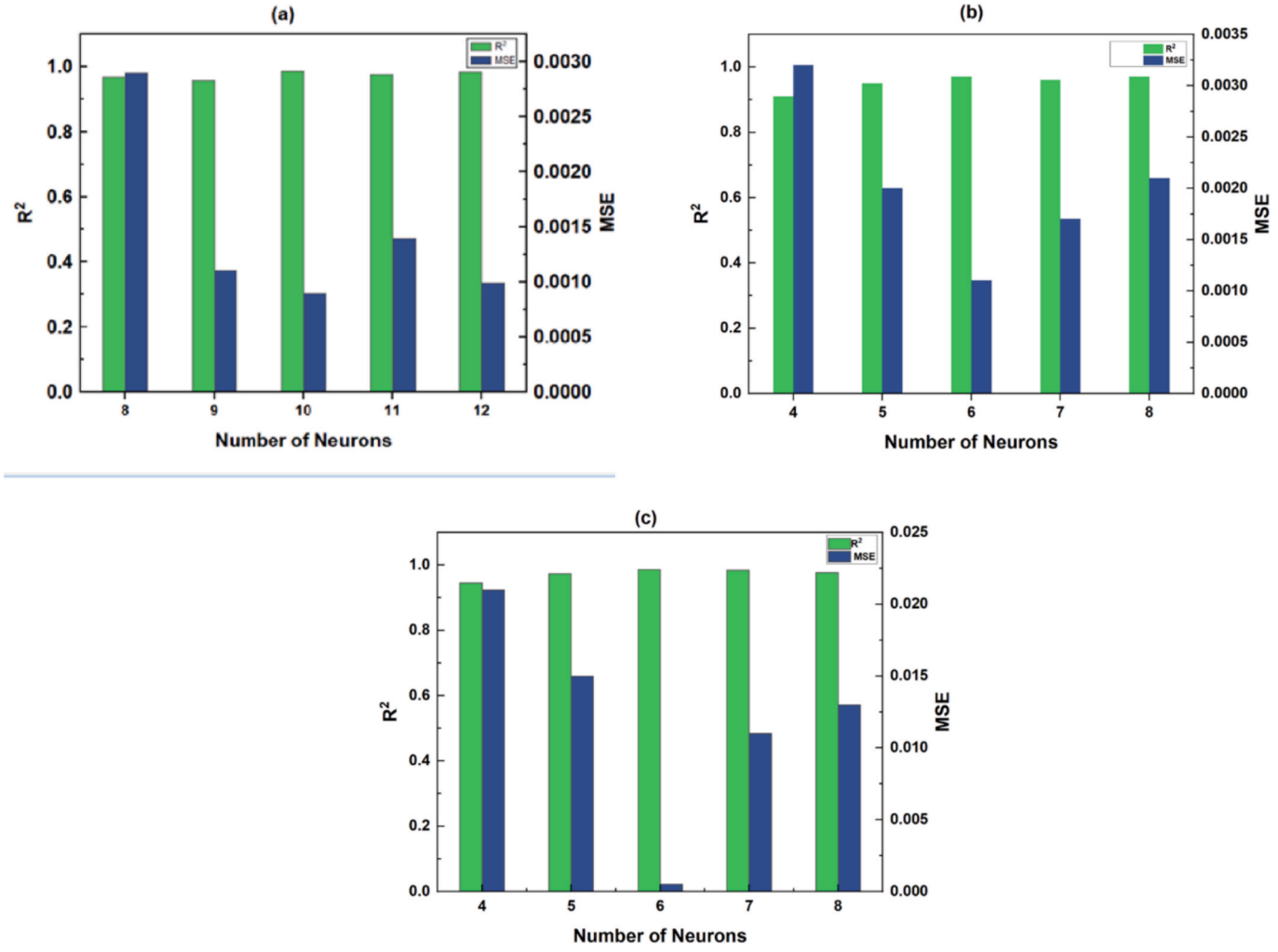


Fig. 6. Effect of hidden-layer neuron number on MLP performance for Model of (a) storage, (b) pressure drop, (c) ohmic loss efficiency.

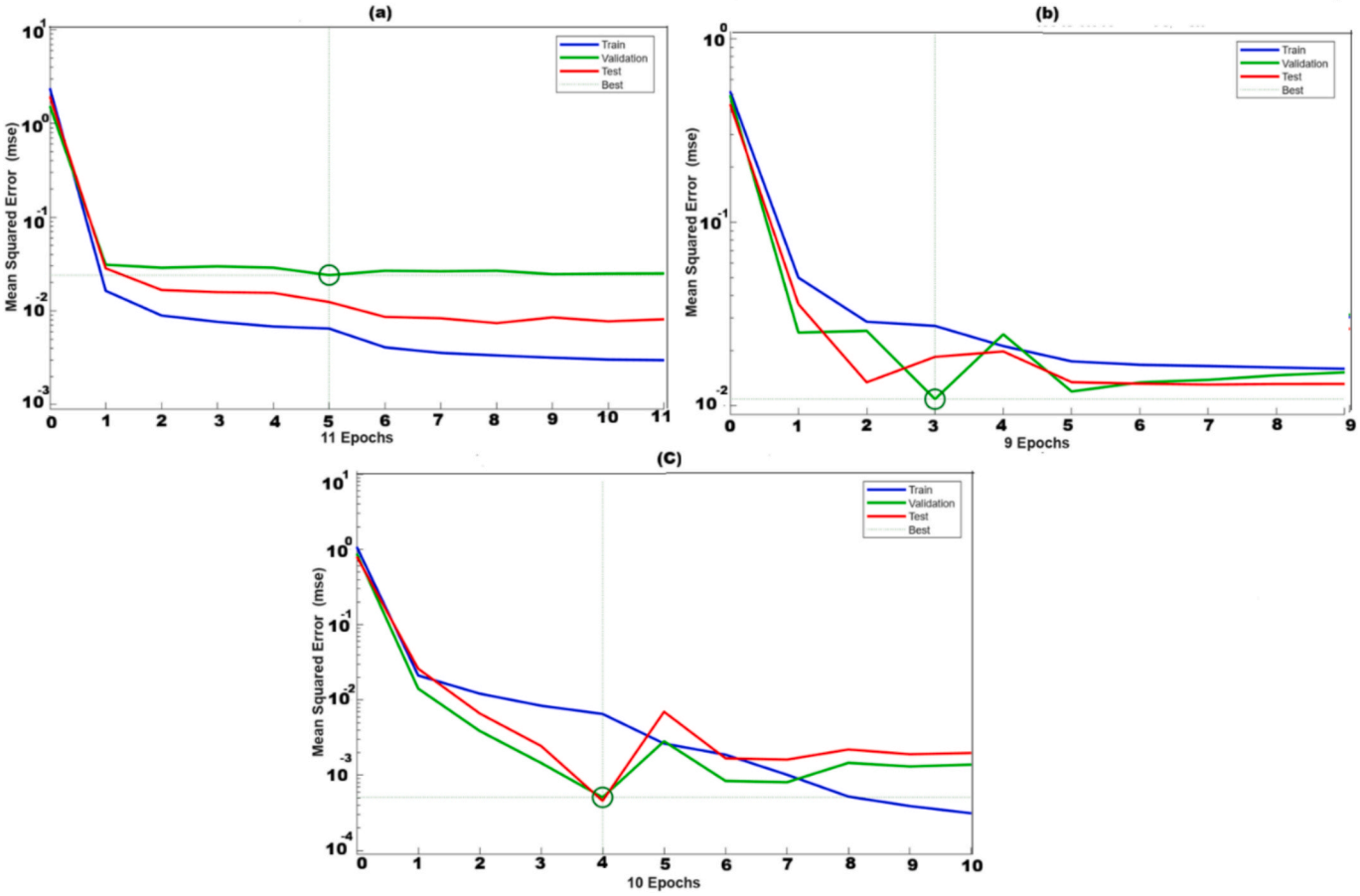


Fig. 7. Learning curves of the three trained MLP models: (a) Storage, (b) Pressure drop, and (c) Ohmic loss. The plots show the mean squared error (MSE) for training (blue), validation (green), and test (red) datasets versus epochs.

curves closely follow the training curves, confirming that the models generalized well. The rapid convergence (3–5 epochs) is consistent with the Levenberg–Marquardt training algorithm, which is known for its fast convergence in small-to-medium MLP networks.

Fig. 8 shows scatter plots comparing the accuracy of the trained MLPs with the CFD models. Also, Tables 3, 4, and 5 show the weights and biases used in the three cases.

Although the MLP model for storage capacity showed high predictive accuracy, it was not included in the optimization phase. Storage in this system is largely proportional to the electrode surface area and does not conflict strongly with the other objectives. Consequently, the optimization was focused on ohmic loss and pressure drop, which exhibit a clearer trade-off and exert a more direct influence on system efficiency. The storage MLP remains useful for evaluating the designs produced by MOO and could be integrated in the future as part of a tri-objective framework.

3.3. *Multi objective optimization of ohmic loss and pressure drop*

Once the surrogate models were trained, the focus shifted to optimizing the design. The results of the simulation study show that ohmic loss and pressure drop (the decisive factors in the evaluation of membraneles electrolyzers) exhibit conflicting behavior. Thus, an increase in pressure drop contributes to a decrease in ohmic loss, and vice versa. This trade-off is shown in Fig. 8.

In Fig. 9, a sensitivity analysis of the decision variables is presented, where each geometrical parameter was varied individually while keeping the others fixed. This allows the isolated influence of each parameter on the objectives to be quantified.

These trends are rooted in the intrinsic hydrodynamic behavior of Tesla valves. The valve geometry enforces asymmetric splitting of the flow: in the forward direction, fluid streams recombine smoothly, while in the reverse direction, junctions promote recirculation and vortex formation that increase resistance. Parameters such as connector width and spacing directly control the strength of these recirculation zones, thereby altering the balance between hydraulic losses and ionic transport. Also, higher diodicity reflects a stronger suppression of reverse flow, which improves uniformity of the forward streamlines and reduces unnecessary mixing. Thus, the observed dependencies of pressure drop and ohmic loss can be understood as manifestations of the Tesla valve's fundamental principle of using geometry, rather than moving parts, to regulate flow resistance.

The results also demonstrate the opposing behavior of ohmic loss and pressure drop. For example, by increasing, the Tesla connections become less effective, contributing to a decrease in pressure drop in the TV electrolyzers but an increase in ionic transport between the electrodes, leading to higher ohmic loss. Fig. 8-b shows that increasing diodicity effectively suppresses internal recirculation and backflow-induced disturbances. As a result, the flow remains more streamlined within each main channel, minimizing hydraulic losses and reducing overall pressure drop. In contrast, increasing the Tesla connection width contributes to higher pressure drop due to enhanced internal recirculation and disturbance; however, it provides more ionic paths. Similarly, decreasing the distance between the connections has the same effect on pressure drop and ohmic loss, comparable to those observed when increasing the Tesla connection width. This sensitivity analysis confirms that all selected variables significantly affect the objectives and, at the same time, highlights their conflicting trends, thereby motivating the

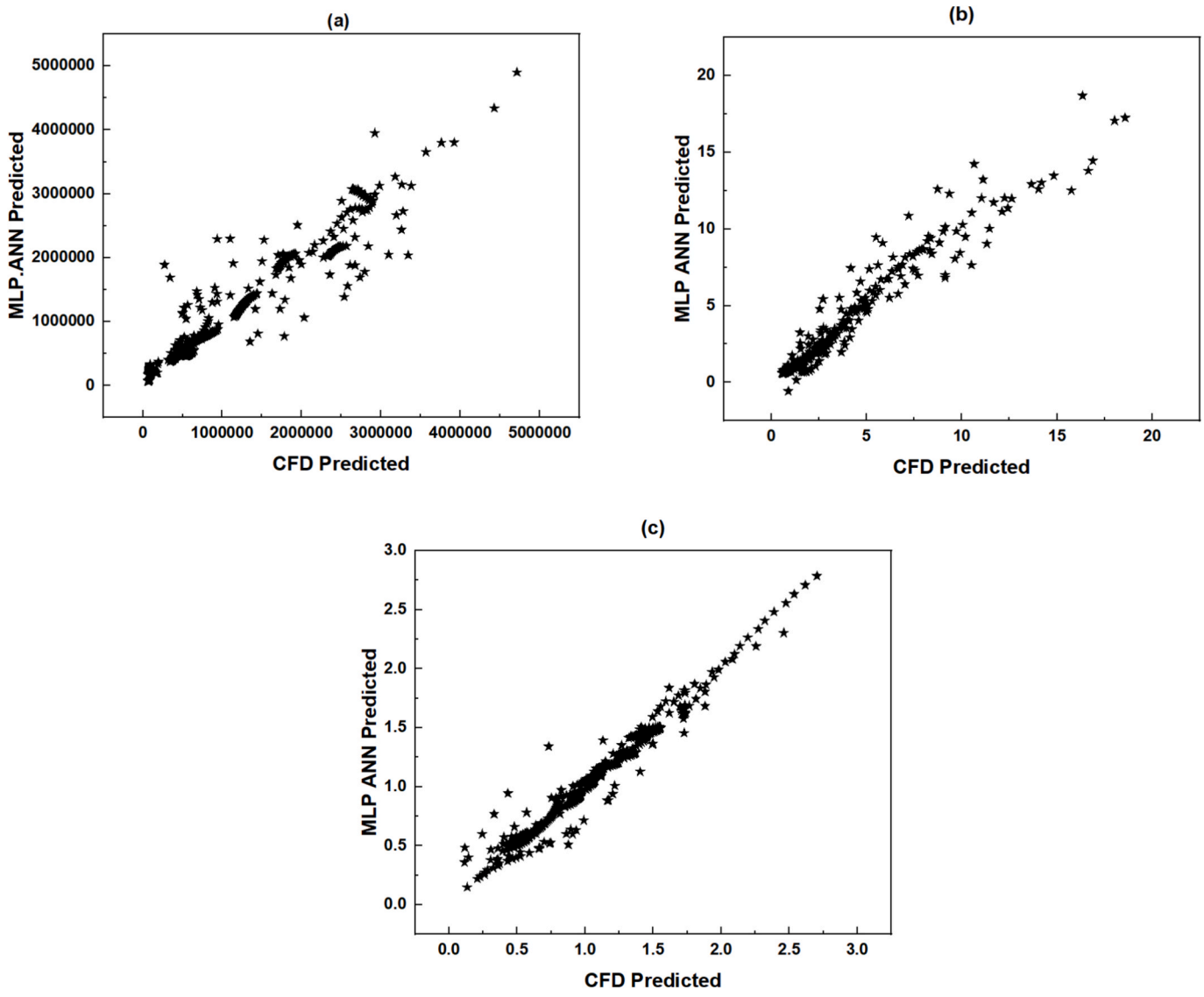


Fig. 8. Comparison of validated CFD and MLP model for (a) storage, (b) pressure drop, (c) ohmic loss.

Table 3
Weights and biases of the MLP for approximation of Storage.

Neuron	Wji We	Wc	Wd	Di	bj	Bk = -0.38173 **Wkj**
W1	0.889267400173930	0.743044251995802	−2.77546887880996	0.018935741652909	−2.669553283943	0.314381382546723
2	−0.39026834500144	0.156697787758655	2.21120189276565	−0.84428657202427	2.490985901350	0.39380730955993
3	1.64143941492029	0.559153987077094	0.871188737121411	−0.70620338339308	−1.599247615344	0.4128675765489
4	−0.17878255123714	−2.10570063336830	0.462552447061185	−0.98317933981714	−0.006439823390	−0.1271596053191
5	1.25444863132400	0.112690806889851	0.38457653620883	2.63880224586244	−0.574442685471	0.25443609444848
6	−0.21756476789100	0.122823383707099	−1.66858471702547	−1.94552671532053	0.8597721079992	0.0971066361622
7	0.376783105394167	−3.00169918320548	2.24313827022997	−1.03387075926881	0.7186523850606	0.2118813747460
8	0.157383332583951	0.048347522293564	0.018029604793154	−2.99832642815957	2.0973563398212	0.5053849059988
9	−2.4924734352520	−1.24417901584091	0.137905508938397	−0.45869084265528	−2.191795085515	−0.359180630472
10	−0.23984006427710	−0.66497308789093	−1.31722655385305	−1.6770368875005	−2.390058692729	0.0563488535391

use of a multi-objective optimization framework.

It is worth noting that the present analysis was conducted under single-phase flow conditions. This method neglect bubble formation and presence in the system during electrolysis. Bubble generation can significantly influence local flow distribution, conductivity, and overall system performance. Future work will address these multiphase effects through coupled experimental and two-phase numerical validation.

To solve this issue, two trained MLP models representing ohmic and pressure drop were employed as surrogate models in a reference function to be minimized. As described earlier, MOO was carried out by using a genetic algorithm. In this optimization, each objective function was considered as a function of decision variables in the MOO process. The genetic algorithm used an initial population size of 600. The objective function, which is based on the surrogate models of ohmic loss and pressure drop, was calculated for each individual population. Subsequently, the solutions were ranked based on their contribution to the

Table 4
Weights and biases of the MLP for approximation of Pressure Drop.

Neuron	Wji				bj	Bk = 1.256108428
	We	Wc	Wd	Di		Wkj
1	−0.21934227	−1.3003373	−1.402717476	−0.28084526	2.67376213495	0.77122191
2	0.387270064	−0.8925078	−0.827151791	1.822281454	2.327311035520	0.379865000
3	−0.02600199	0.0768780	2.427300863	0.086018639	3.29758899821	−1.84874287
4	−0.24207271	−0.02503865	−1.08250830	2.252155022	1.691614210845	−1.29473068
5	0.38116624	0.12990981	0.508451994	−0.826607176	−0.70679727150	2.6490350529
6	−2.71179251	1.691667152	−3.351901325	1.0115985050	−1.1298666606	0.1604946211

Table 5
Weights and biases of the MLP for approximation of Ohmic Loss.

Neuron	Wji				bj	Bk = 5.62944558
	H	Wc	Wd	Di		Wkj
1	−3.55940570	5.067249355	−1.77624372	−2.22793620	0.17581969	−0.17162013
2	−1.23461818	2.221845539	0.075378816	1.954023410	−0.4184216	−0.010144707
3	2.765551378	−5.348977011	3.064466493	0.348094243	5.43010959	0.078458484
4	−0.507101440	−7.464599472	9.389117747	3.844301545	−1.23896969	−2.7559866321
5	0.729035302	−7.398638102	9.275835103	3.804732938	−0.03364374	2.7717631938
6	0.15018852	6.417720430	−0.086215046	−0.067568512	6.89044618	−6.3484840053

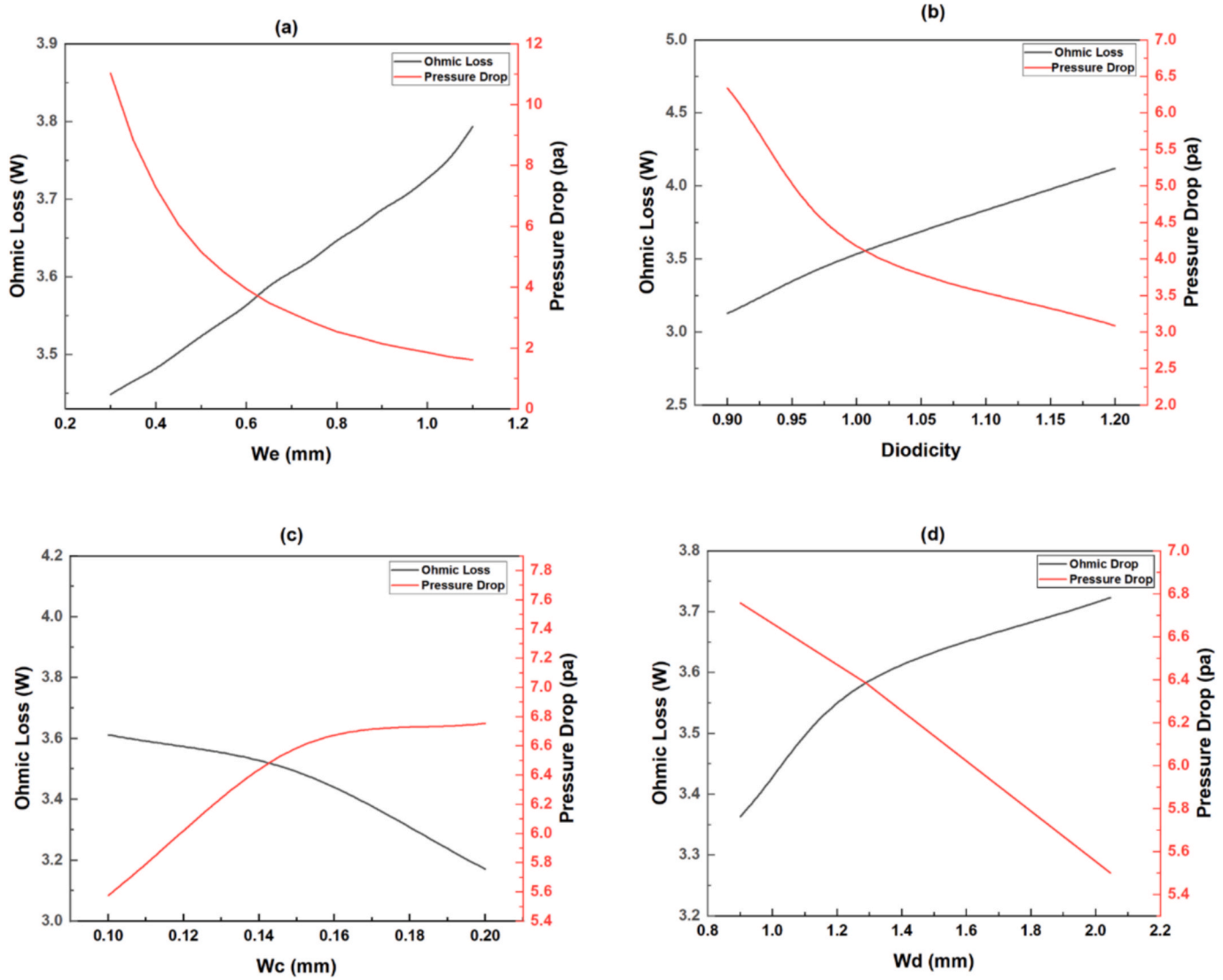


Fig. 9. Sensitivity analysis of the decision variables showing the opposing behavior of ohmic loss and pressure drop. Each parameter was varied individually while the others were held constant to isolate its influence: (a) We, (b) diodicity, (c) Wc, and (d) Wd.

Pareto front.

A range of parameters, including population size and mutation rate, were adjusted to achieve the algorithm's best performance. The results are presented in Fig. 10 which plots the Pareto front, and provide insight into the trade-offs between the objectives. This visualization supports informed decision-making when selecting an optimal solution. Also, all the corresponding geometrical specifications are listed in the table in Supplementary III.

The shape of the Pareto front confirms that improving one objective often entails compromising the other. This provides flexibility in design decisions depending on whether minimizing pressure drop or ohmic loss is prioritized.

To determine the most balanced configuration among the Pareto-optimal solutions, the Technique for Order of Preference by Similarity to Ideal Solution (TOPSIS) was applied as a multi-criteria decision-making (MCDM) method[41]. The objectives were ohmic loss and pressure drop, both treated as cost criteria and normalized using min–max scaling. Equal importance (50/50 weighting) was assigned to reflect their comparable influence on the system's energy performance.

The analysis was performed on 60 matched geometry and objective pairs. The best-performing design exhibited an ohmic loss of 4.069 V and a pressure drop of 6.169 Pa, attaining the highest TOPSIS score. This configuration corresponds to a channel height of 1.708 mm, tesla connection width Wc of 0.200 mm, Wd of 1.012 mm, and Di of 1.618. this point is demonstrated by a red star in figure 9.

Comparatively, the experimental Tesla-valve based electrolyzer in our previous work reference here proves feasibility and reports operating points of 300 mA·cm^{-2} at ultra-low flow with safe gases separation, and ~ 13 % H_2 productivity via diodicity-guided terms. The ML-aided study extends this by quantifying the design space and exposing the trade-off surface between ohmic loss and pressure drop across realistic Tesla-valve geometries, see Table S2 is Supplementary III.

This result represents an effective trade-off between required pumping power and voltage and can guide future experimental validations or scale-up efforts.

4. Conclusion

In this work, a machine learning-based framework was developed to optimize a Tesla valve membraneless electrolyzer. Three multi-layer perceptron artificial neural network models were trained to predict storage capacity, pressure drop, and ohmic loss from geometrical inputs. These models were built on COMSOL simulations data and showed good predictive accuracy. An inverse MLP-GA tool was also created to find the Tesla geometry that gives a target diodicity, helping to avoid repetition in the training data. The trained surrogate models were used in a multi-objective optimization to explore the best trade-off between ohmic loss and pressure drop. Results indicated that reducing one can increase the other emphasizing the necessity of a balanced designed strategy. The storage model was not included in the optimization because its value mainly depends on electrode size and does not conflict with the other two outputs.

A total of 60 geometric configurations were introduced within a design space of 0.25–2.1 mm for main channels, 0.04–0.2 mm for the Tesla connection width, 0.41–2.5 mm for the distance between connections, and 0.9–1.7 for the diodicity. These designs contributed to a range of 1.4 V in ohmic loss and 7 Pa in pressure drop. The multi criteria decision making using TOPSIS identified an optimal configuration with channel width of 1.708 mm, tesla connection width of 0.200 mm, distance between connections of 1.012 mm, and Diodicity of 1.618, achieving the best efficiency.

The proposed framework reduced simulation time and provided meaningful design insights. In future work, this approach can be extended to include more objectives or be applied to other microfluidic or electrochemical systems.

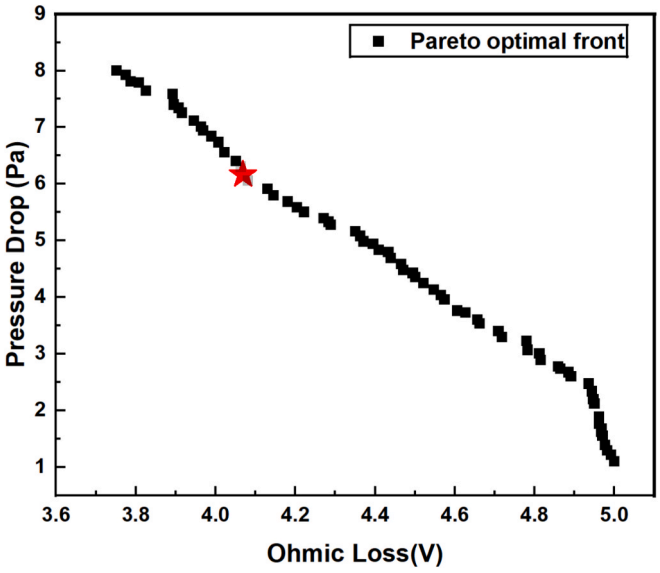


Fig. 10. Pareto-optimal front of optimal pressure drop and ohmic loss.

Funding.

This project has received funding from the European Union's Horizon 2020 research and innovation programme under the Marie Skłodowska-Curie Grant Agreement No. 945,413 and from the Universitat Rovira i Virgili (URV) under project ID: 2021MFP-COFUND-23-UE. Project PID2022-141499OB-100, funded by MICIU/AEI/https://doi.org/10.13039/501100011033/ and by FEDER/UE.

CRediT authorship contribution statement

Mohammadali Zoljalali: Writing – original draft, Visualization, Validation, Software, Methodology, Investigation, Formal analysis, Data curation, Conceptualization. **Richard Ahorsu:** Writing – review & editing, Supervision, Investigation, Formal analysis. **Francesc Díaz:** Supervision. **Magdalena Aguiló:** Supervision. **Xavier Mateos:** Writing – review & editing, Supervision, Resources, Project administration, Investigation.

Declaration of competing interest

The authors declare that they have no known competing financial interests or personal relationships that could have appeared to influence the work reported in this paper.

Appendix A. Supplementary data

Supplementary data to this article can be found online at https://doi.org/10.1016/j.fuel.2025.137328.

Data availability

Data will be made available on request.

References

[1] A. Manzotti, M. J. Robson, and F. Ciucci, "Recent developments in membraneless electrolysis," Apr. 01, 2023, *Elsevier B.V.* doi: 10.1016/j.cogsc.2023.100765.
[2] Pang X, Davis JT, Harvey AD, Esposito DV. Framework for evaluating the performance limits of membraneless electrolyzers. Energy Environ Sci Oct. 2020; 13(10):3663–78. https://doi.org/10.1039/d0ee02268c.
[3] Hadikhani P. Investigating bubble-induced overpotential, current non-uniformity, and bubble distribution in flow-based water electrolyzers: a numerical study. Int J Hydrogen Energy Sep. 2024;84:793–802. https://doi.org/10.1016/j.ijhydene.2024.08.231.

[4] S. Razavi Bazaz, A. Mashhadian, A. Ehsani, S. C. Saha, T. Krüger, and M. Ebrahimi Warkiani, "Computational inertial microfluidics: a review," Mar. 21, 2020, *Royal Society of Chemistry*. doi: 10.1039/c9lc01022j.

[5] Hashemi SMH, et al. A versatile and membrane-less electrochemical reactor for the electrolysis of water and brine. Energy Environ Sci May 2019;12(5):1592–604. https://doi.org/10.1039/c9ee00219g.

[6] Zoljalali M, Ahorsu R, Díaz F, Aguiló M, Mateos X. Membraneless electrolyzer designed using the tesla valve concept for hydrogen production. Int J Hydrogen Energy Mar. 2025;113:535–49. https://doi.org/10.1016/j.ijhydene.2025.02.235.

[7] O. A. Ibrahim, M. Navarro-Segarra, P. Sadeghi, N. Sabaté, J. P. Esquivel, and E. Kjeang, "Microfluidics for Electrochemical Energy Conversion," Apr. 13, 2022, *American Chemical Society*. doi: 10.1021/acs.chemrev.1c00499.

[8] Di Carlo D, Edd JF, Humphry KJ, Stone HA, Toner M. "Particle Segregation and Dynamics in Confined Flows" 2009.

[9] Rajora A, Haverkort JW. An analytical multiphase flow model for parallel plate electrolyzers. Chem Eng Sci Oct. 2022;260. https://doi.org/10.1016/j.ces.2022.117823.

[10] Rajora A, Haverkort JW. An analytical model for the velocity and gas fraction profiles near gas-evolving electrodes. Int J Hydrogen Energy Aug. 2023;48(71):27450–63. https://doi.org/10.1016/j.ijhydene.2023.03.154.

[11] Hadikhani P, et al. Inertial manipulation of bubbles in rectangular microfluidic channels. Lab Chip Apr. 2018;18(7):1035–46. https://doi.org/10.1039/c7lc01283g.

[12] Hadikhani P, Hashemi SMH, Schenk SA, Psaltis D. A membrane-less electrolyzer with porous walls for high throughput and pure hydrogen production. Sustain Energy Fuels May 2021;5(9):2419–32. https://doi.org/10.1039/d1se00255d.

[13] D. V. Esposito, "Membraneless Electrolyzers for Low-Cost Hydrogen Production in a Renewable Energy Future," Dec. 20, 2017, *Cell Press*. doi: 10.1016/j.joule.2017.07.003.

[14] O'Neil GD, Christian CD, Brown DE, Esposito DV. Hydrogen Production with a simple and Scalable Membraneless Electrolyzer. J Electrochem Soc 2016;163(11):F3012–9. https://doi.org/10.1149/2.0021611jes.

[15] Yan X, et al. A membrane-free flow electrolyzer operating at high current density using earth-abundant catalysts for water splitting. Nat Commun 2021;12(1):Dec. https://doi.org/10.1038/s41467-021-24284-5.

[16] Nabavi SR, Jafari MJ, Wang Z. Deep Learning aided Multi-Objective Optimization and Multi-Criteria Decision making in thermal Cracking Process for Olefines Production. J Taiwan Inst Chem Eng Nov. 2023;152. https://doi.org/10.1016/j.jtice.2023.105179.

[17] Konak A, Coit DW, Smith AE. Multi-objective optimization using genetic algorithms: a tutorial. Reliab Eng Syst Saf Sep. 2006;91(9):992–1007. https://doi.org/10.1016/j.ress.2005.11.018.

[18] Zhuang Y, Cui P, Long R, Liu W, Liu Z. Multi-objective optimization of channel structure for a proton exchange membrane water electrolysis cell. Int J Hydrogen Energy Jan. 2024;49:337–52. https://doi.org/10.1016/j.ijhydene.2023.08.026.

[19] Zhu Q, Cheng W, Yang J, Sun H, Liu W, Li H. Optimizing efficiency of proton exchange membrane electrolyzer system based on multiphysics model and differential evolution strategy. J Power Sources Nov. 2024;621. https://doi.org/10.1016/j.jpowsour.2024.235270.

[20] Chen J, Lv H, Shen X, Zhang C. Multi-objective optimization design and sensitivity analysis of proton exchange membrane electrolytic cell. J Clean Prod Jan. 2024;434. https://doi.org/10.1016/j.jclepro.2023.140045.

[21] Ding R, et al. Guiding the Optimization of Membrane Electrode Assembly in a Proton Exchange Membrane Water Electrolyzer by Machine Learning Modeling and Black-Box Interpretation. ACS Sustain Chem Eng Apr. 2022;10(14):4561–78. https://doi.org/10.1021/acssuschemeng.1c08522.

[22] Nikzad A, Iranshahi D, Ranjbaran M. Improvement in Ammonia, Hydrogen, and Methyl Formate Synthesis Process by Employing Multiobjective Optimization of a Novel Multifunctional Membrane Reactor. Energy Fuels 2023;37(4):3280–93. https://doi.org/10.1021/acs.energyfuels.2c03550.

[23] Saeedi R, Iranshahi D. Multi-objective optimization of thermally coupled reactor of CCR naphtha reforming in presence of SO2 oxidation to boost the gasoline octane number and hydrogen. Fuel 2017;206:580–92. https://doi.org/10.1016/j.fuel.2017.04.024.

[24] X. Chen *et al.*, "Machine Learning in Proton Exchange Membrane Water Electrolysis – Part I: A Knowledge-Integrated Framework," Jan. 2024, [Online]. Available: http://arxiv.org/abs/2404.03660.

[25] Wang Z, Li J, Rangaiah GP, Wu Z. Machine learning aided multi-objective optimization and multi-criteria decision making: Framework and two applications in chemical engineering. Comput Chem Eng Sep. 2022;165. https://doi.org/10.1016/j.compchemeng.2022.107945.

[26] A. Morales-Hernández, I. Van Nieuwenhuyse, and S. Rojas Gonzalez, "A survey on multi-objective hyperparameter optimization algorithms for machine learning," *Artif Intell Rev*, vol. 56, no. 8, pp. 8043–8093, Aug. 2023, doi: 10.1007/s10462-022-10359-2.

[27] Shahriari S, Iranshahi D. Simultaneous OPEX and carbon footprint reduction with hydrogen enhancement in autothermal reforming: a machine learning–based surrogate modeling and optimization framework. Results Eng 2025;27. https://doi.org/10.1016/j.rineng.2025.106286.

[28] "The Tertiary Current Distribution, Nernst-Planck Interface".

[29] Sadrara M, Khorrami MK. Principal component analysis–multivariate adaptive regression splines (PCA-MARS) and back propagation-artificial neural network (BP-ANN) methods for predicting the efficiency of oxidative desulfurization systems using ATR-FTIR spectroscopy. Spectrochim Acta A Mol Biomol Spectrosc Nov. 2023;300. https://doi.org/10.1016/j.saa.2023.122944.

[30] S. Ariffin, A. Karim, N. Saad, and R. Kannan, "Studies in Systems, Decision and Control 320 Advanced Methods for Processing and Visualizing the Renewable Energy A New Perspective from Signal to Image Recognition." [Online]. Available: http://www.springer.com/series/13304.

[31] Movassagh AA, et al. Artificial neural networks training algorithm integrating invasive weed optimization with differential evolutionary model. J Ambient Intell Hum Comput May 2023;14(5):6017–25. https://doi.org/10.1007/s12652-020-02623-6.

[32] H. P. Gavin, "The Levenberg-Marquardt algorithm for nonlinear least squares curve-fitting problems," 2024.

[33] A. Hemmati-Sarapardeh, A. Varamesh, M. M. Husein, and K. Karan, "On the evaluation of the viscosity of nanofluid systems: Modeling and data assessment," 2018, *Elsevier Ltd*. doi: 10.1016/j.rser.2017.07.049.

[34] Abdollahzadeh B, Gharehchopogh FS. A multi-objective optimization algorithm for feature selection problems. Eng Comput Aug. 2022;38:1845–63. https://doi.org/10.1007/s00366-021-01369-9.

[35] Petchrompo S, Coit DW, Brintrup A, Wannakrairot A, Parlikad AK. A review of Pareto pruning methods for multi-objective optimization. Comput Ind Eng May 2022;167. https://doi.org/10.1016/j.cie.2022.108022.

[36] Deng W, et al. An enhanced fast non-dominated solution sorting genetic algorithm for multi-objective problems. Inf Sci (N Y) Mar. 2022;585:441–53. https://doi.org/10.1016/j.ins.2021.11.052.

[37] A. Sohail, "Genetic Algorithms in the Fields of Artificial Intelligence and Data Sciences," Aug. 01, 2023, *Springer Science and Business Media Deutschland GmbH*. doi: 10.1007/s40745-021-00354-9.

[38] Sharifi MR, Akbarifard S, Qaderi K, Madadi MR. A new optimization algorithm to solve multi-objective problems. Sci Rep 2021;11(1):Dec. https://doi.org/10.1038/s41598-021-99617-x.

[39] I. Costa-Carrapiço, R. Raslan, and J. N. González, "A systematic review of genetic algorithm-based multi-objective optimisation for building retrofitting strategies towards energy efficiency," Mar. 01, 2020, *Elsevier Ltd*. doi: 10.1016/j.enbuild.2019.109690.

[40] P. Hnin Thike, Z. Zhao, P. Shi, and Y. Jin, "Significance of artificial neural network analytical models in materials' performance prediction," *Bulletin of Materials Science*, vol. 43, 2024, doi: 10.1007/s12034-020-02154-yS.

[41] Rachman AP, Ichwania C, Mangkuto RA, Pradipta J, Koerniawan MD, Sarwono J. Comparison of multi-criteria decision-making methods for selection of optimum passive design strategy. Energ Buildings Jul. 2024;314. https://doi.org/10.1016/j.enbuild.2024.114285.